

ZnV₂O₄-Textured Carbon Composite Contacting a ZIF-8 MOF Layer for a High Performance Non-Aqueous Zinc-Ion Battery

Souvik Naskar^[a] and Melepurath Deepa^{*[b]}

Non-aqueous zinc-ion battery (ZIB) comprising a zinc vanadate@textured carbon ($\text{ZnV}_2\text{O}_4@\text{TC}$) composite cathode and Zn-anode demonstrates an improved Zn(II)-ion storage response, in terms of cyclability (230 mAh g⁻¹ after 200 cycles, 84.9% retention) and rate capability compared to pristine ZnV_2O_4 (175 mAh g⁻¹ after 200 cycles, 45.4% retention). TC reduces the aggregation of ZnV_2O_4 nanoparticles, allows abundant interaction with electrolyte, affords short ion diffusion pathways, serves as electrically conducting interconnects, and buffers the volume alterations thus imparting rapid kinetics and improved cycling stability. This performance is even better by the inclusion of a ZIF-8 metal-organic framework (MOF) layer at the

separator, facing the cathode. ZIF-8 due to its nanoporous structure encompassing Zn–N based polyhedral clusters, efficiently confines Zn(II) ions at cathode during discharge and allows their facile diffusion through its open channels during charge thus maximizing Zn(II) ion storage capacity and reversibility and its highly crystalline robust structure also enhances the ZIB durability. This achievement is in line with the development of cost-effective, easily implementable non-aqueous ZIB that avoids the issues associated with aqueous electrolyte of limited potential stability window, corrosion of current collectors over time, and cell degradation and also offers long term stability and capacity.

Introduction

Among the various rechargeable batteries currently being explored in the energy storage space, zinc-ion batteries (ZIBs) are attractive, due to the natural abundance, low cost, negligible toxicity, high air-stability and safety of Zn compared to Na or Li, as in Na/Li-ion batteries.^[1–5] The large theoretical gravimetric capacity (820 mAh g⁻¹), the high oxidation potential [+0.76 V versus normal hydrogen electrode (NHE)], the ability to transfer two electrons per gram equivalent of zinc thus enhancing energy density and the ecologically friendly nature are additional benefits incurred by the use of Zn as an anode in ZIBs.^[1–3] The cathode in a ZIB is required to have an open structure enabling easy intercalation and deintercalation of Zn(II) ions, during discharging and charging processes, to maximize energy storage via diffusion and Faradaic mechanisms. A variety of crystalline transition metal oxides^[6–10] and Prussian blue analogues^[11–14] endowed with channel dimensions in excess of 1.5 Å [which is approximately twice the ionic radius of Zn(II) ion] have been deployed as cathodes in ZIBs.

Vanadium based oxides have been widely used as hosts in aqueous ZIBs due to their layered structures and wide inter-

layer separations and some examples worthy of note are: $\text{Zn}_{0.3}\text{V}_2\text{O}_5 \cdot 1.5\text{H}_2\text{O}$, which delivered a capacity of 426 mAh g⁻¹ at 0.2 A g⁻¹ and exhibited a cycling stability with a capacity retention of 96% over 20000 cycles at 10 A g⁻¹,^[15] porous $\text{Mg}_{0.34}\text{V}_2\text{O}_5 \cdot 0.84\text{H}_2\text{O}$ nanobelts which produced a capacity of 353 mAh g⁻¹ at 100 mA g⁻¹, with ~97% capacity retention for 2000 cycles,^[16] $\text{Na}_2\text{V}_6\text{O}_{16} \cdot 3\text{H}_2\text{O}$ nanorods that offered a specific energy of 90 Wh kg⁻¹ at a specific power of 15.8 kW kg⁻¹,^[17] a commercial V_2O_5 cathode, which showed a reversible capacity of 470 mAh g⁻¹ at 0.2 A g⁻¹ and a long-term cyclability with 91% capacity retention over 4000 cycles at 5 A g⁻¹,^[18] ZnVOH/carbon cloth based flexible ZIB that showed a high discharge capacity of 184 mAh g⁻¹ at 10 A g⁻¹ after 170 cycles^[19] and $\text{NaV}_3\text{O}_8 \cdot 1.5\text{H}_2\text{O}$ nanobelts, with a high reversible capacity of 380 mAh g⁻¹ and capacity retention of 82% over 1000 cycles.^[20]

Most of the above described reports on ZIBs are based on aqueous electrolytes,^[15–21] but i) their narrow electrochemical potential stability, limited by the decomposition potential of water at ~1.23 V, thereby restricting the operational voltage of the ZIB, ii) the competitive insertion of H⁺ ions in an acidic aqueous medium along with Zn²⁺, and iii) the possible undesirable side reactions of water with cathode materials can have deleterious effects on the capacity and lifespan of ZIBs, thus rendering them to rather unsuitable for scale up or any real-world applications. These issues can be addressed by the use of non-aqueous electrolytes, but at the expense of Zn(II) storage capacity. Typically, the best values are less than 200 mAh g⁻¹, plausibly due to a high activation energy associated with charge transfer at the electrolyte/cathode interface and the corresponding sluggish ion-transfer kinetics.^[22] By using two Zn(II) ion-based host materials, at the cathode, not as a composite, but as independent layers with

[a] S. Naskar
Department of Chemistry
Indian Institute of Technology Hyderabad
Kandi, Sangareddy, Telengana-502284, India

[b] Prof. M. Deepa
Department of Chemistry
Indian Institute of Technology Hyderabad
Kandi, Sangareddy, Telengana-502284, India
E-mail: mdeepa@chy.iith.ac.in

 Supporting information for this article is available on the WWW under <https://doi.org/10.1002/batt.202100364>

specific roles, these problems can be surmounted to some extent. Zinc vanadate (ZnV_2O_4), which has a 2D layered structure conducive for Zn(II) ion ingress and egress as a cathode is coupled with a Zn-metal organic framework (MOF) applied over the separator, thus providing the spatial arrangement ideal for Zn(II) ion confinement at the cathode side during discharge. In the past, an aqueous ZIB containing a ZnV_2O_4 spinel cathode, wherein a reversible capacity of 312 mAh g^{-1} with retention of 206 mAh g^{-1} over 1000 cycles at a high rate of 10 C has been reported.^[23] Here, a substantial improvement has been achieved in comparison, with a composite cathode of ZnV_2O_4 and textured carbon derived from a low cost bio-source of betel nut shells, and by deploying a ZIF-8 (zeolitic imidazolate framework) layer at the separator that allows easy inflow and outflow of Zn(II) ions during discharge and charge, thus maximizing capacity and durability. In their study,^[23] the operational voltage window was $\sim 1.1\text{--}1.2 \text{ V}$, here it is 1.6 V , thus improving the energy density. Due to their organized porosity, resistance to thermal alterations and chemical stability, ZIFs are ideal for the application to an energy storage device.^[24\text{--}26] Furthermore, the ZIB here encompasses an organic electrolyte, overcomes the issues posed by aqueous media, allowing the attainment of a stable voltage window of 1.6 V , long term cycle life, and no intercalation of hydronium ions. This ZIB configuration opens up possibilities to use metal ion conducting MOF overlayers at the separator as a generic strategy for developing batteries with high ion-storage capacity, reversibility and endurance.

Results and Discussion

Morphology and lattice scale features of cathode materials

Figure 1 shows the FE-SEM images the cathode materials. Pristine ZnV_2O_4 , as can be seen from Figure 1(a, a') is composed of irregular shaped interconnected particles, conducive for unhindered charge transport during charge-discharge, across the cross-section of the active material, when used as a cathode in a ZIB. The images of TC (Figure 1b, b') show a textured flaky morphology suitable for maximum ion-adsorption thus, supporting more ion-insertion into the composite of $\text{ZnV}_2\text{O}_4@\text{TC}$ during electrochemical cycling. The images of the $\text{ZnV}_2\text{O}_4@\text{TC}$ composite (Figure 1c, c') reveal a mixed morphology, comprising of the ZnV_2O_4 particles mingling with the 3D-TC shapes. The presence of juxtaposed oxide and the carbon structures implies that electron transfer between them is expected to be unobstructed and facile, which can enhance the kinetics of the electrochemical reactions, and consequently the rate capability.

The high-resolution TEM images of pristine ZnV_2O_4 (Figure 1d-f), clearly shows the highly crystalline nature of the material, for the particles are constituted by a network of interlinked nanocrystallites of the oxide, with dimensions in the range of 5 to 10 nm. The nanocrystallites do not have distinct grain boundaries and they are occasionally overlapping, but the lattice fringes are distinctly visible, especially in Figure 1(f). The inter-fringe distances are ~ 0.25 and $\sim 0.5 \text{ nm}$, which are

associated with the (311) and (111) planes of face-centered cubic (fcc) ZnV_2O_4 (JCPDS: 75-0318). Selected area electron diffraction pattern (SAED) of ZVO (inset of Figure 1f), shows bright concentric rings, which are indexed to the (220), (222), (331), (440) and (442) planes. ZnV_2O_4 , has a spinel structure wherein the cations Zn and V occupy the tetrahedral (8a) sites and octahedral (16d) sites respectively, and the anion: O^{2-} occupies the 32e sites, creating a cubic close packed array. Spinels have a high crystal porosity with multiple vacant octahedral and tetrahedral sites, for Zn and V cations only occupy $1/8^{\text{th}}$ of the tetrahedral sites and $1/2$ of the octahedral sites.^[27] Hence, the empty sites can accommodate the foreign ions from the electrolyte with ease. During discharge, the Zn(II) ions are therefore, anticipated to effortlessly intercalate into the oxide matrix. The composite also has TC, which has a nanoporous flaky structure, with pore sizes that vary from 20 to 30 nm (Figure 1g). The $\text{ZnV}_2\text{O}_4@\text{TC}$ composite (Figure 1h, i) shows the ZnV_2O_4 nanocrystallites co-existing with the misshaped TC particles. This intimate contact between the oxide and the TC facilitates electron transfer from TC to ZVO, during charge or discharge, thereby improving the rate of redox reactions, a benefit that is unavailable when ZVO is used as the sole active material. Inter-fringe distances of ~ 0.25 and $\sim 0.3 \text{ nm}$ are observed, aligning with the (311) and (220) planes of ZVO, implying that ZVO is able to preserve its crystal structure, in spite of the inclusion of the proximal textured carbon.

XRD and Raman studies of cathode materials

XRD and Raman spectra of pristine ZnV_2O_4 , TC and $\text{ZnV}_2\text{O}_4@\text{TC}$ composite are shown in Figure 2. XRD pattern of pristine ZnV_2O_4 (Figure 2a) exhibits a cluster of intense peaks at $2\theta = 17.00^\circ, 30.65^\circ, 36.17^\circ, 43.73^\circ, 54.27^\circ, 57.82^\circ, 63.44^\circ, 71.70^\circ$ and 74.86° , well indexed to the (111), (220), (311), (400), (422), (511), (440), (620) and (530) planes of a cubic face-centered ZVO phase with the $\text{Fd}\bar{3}\text{m}$ space group (JCPDS: 75-0318). These planes correspond to d -spacings of 4.85, 2.97, 2.53, 2.10, 1.72, 1.62, 1.48, 1.33 and 1.28 \AA .^[23,28,29] The data agrees well with the lattice scale imaging results. The XRD pattern of textured carbon shows two broad peaks at $2\theta = 25.6^\circ$ ($d: 3.34 \text{ \AA}$) and 43.3° ($d: 2.09 \text{ \AA}$), which match with the (002) and (100) planes of hexagonal graphite (JCPDS: 75-1621). The $\text{ZnV}_2\text{O}_4@\text{TC}$ composite shows peaks predominantly from ZVO, and only one strong broad peak at 25.2° is observed from TC. The peaks show slight shifts with respect to pristine ZVO, possibly due to van der Waals or electrostatic interactions between ZVO and TC.

Raman spectrum of pristine ZnV_2O_4 (Figure 2b) shows distinctive peaks at $231, 367$ and 512 cm^{-1} which are assigned to the $\text{F}_{2g(1)}$, the doubly degenerate E_g and the $\text{F}_{2g(2)}$ modes. For the spinel lattice, the least frequency Raman active mode of $\text{F}_{2g(1)}$ is assigned to the total translation of ZnO_4 unit.^[30] The higher frequency peaks at $784, 838$ and 889 cm^{-1} are attributed to the different variants of the Raman active A_{1g} mode. Owing to the nearly same electronegativities of Zn and V, the Zn–O

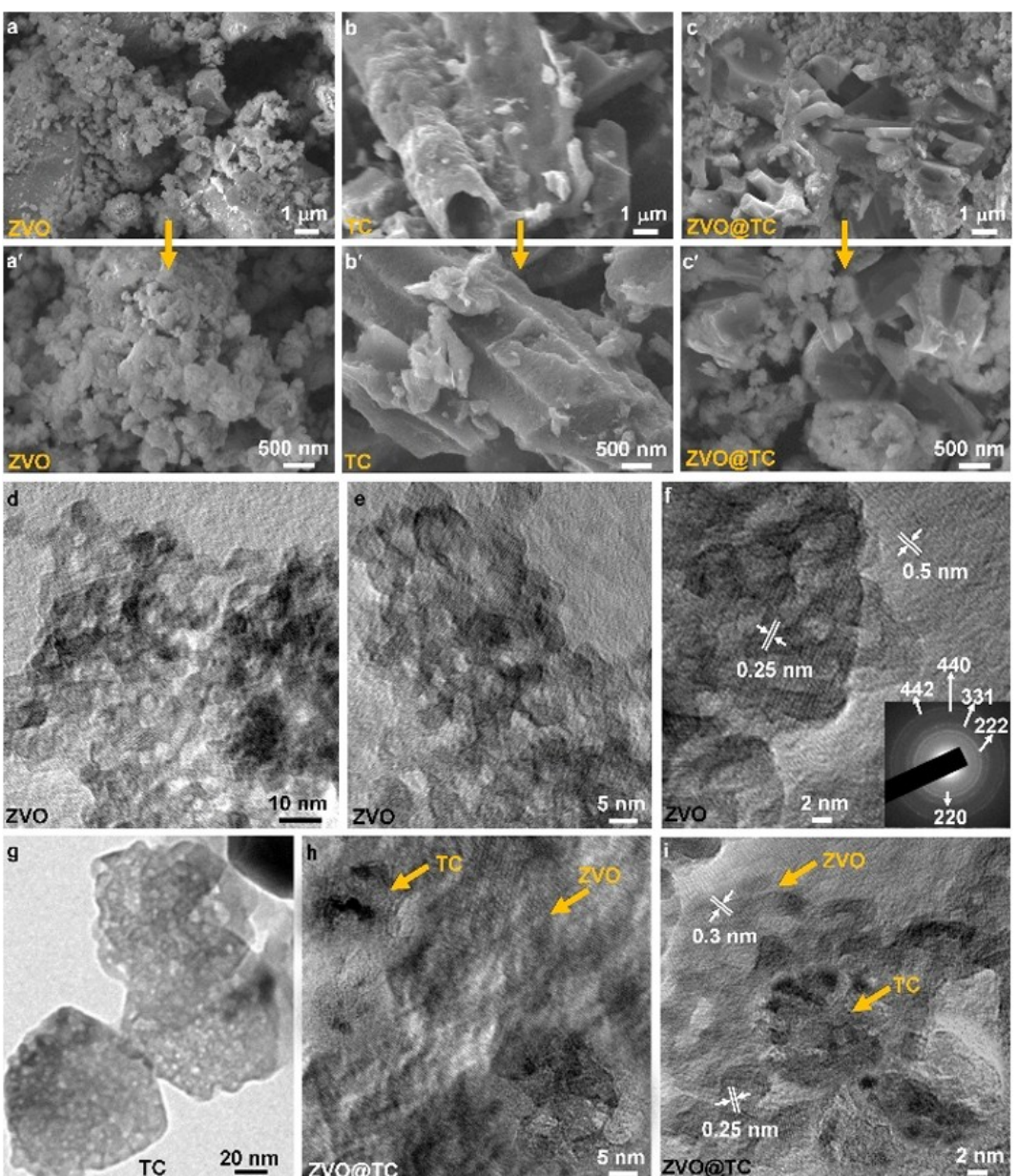


Figure 1. FE-SEM images of a, a') ZnV_2O_4 , b, b') TC and c, c') ZnV_2O_4 @TC composite. TEM images of d–f) ZnV_2O_4 , g) TC and h, i) ZnV_2O_4 @TC composite. Inset of f) is a SAED pattern of ZnV_2O_4 .

and V–O bonds have roughly equivalent strengths, and although the A_{1g} mode is ascribed to the symmetric breathing vibration of ZnO_4 unit, the V–O vibrations also contribute to this mode. In the spinel structure, while the ZnO_4 tetrahedron has an ideal geometry, but the VO_6 octahedron is likely to be distorted, ensuing in the broadness of the A_{1g} mode. The strong peak at 838 cm^{-1} is due to the V–O bond vibrations. These assignments are in good agreement with those reported for ZVO prepared from a solid-state reaction at high temperature using ZnO and V_2O_3 .^[30] Raman spectrum of the carbon nanomaterial, TC shows the D-band and the G-band at 1349 and 1566 cm^{-1} . The D-band corresponds to the breathing mode of A_{1g} symmetry, the out-of-plane vibrations of structural defects (due to the oxygen functionalities flanked to the sp^3 hybridized

carbons) and requires the presence of full-six-membered rings. The G-band has a E_{2g} symmetry and arises from the in-plane vibrations of sp^2 bonded carbon atoms in the graphitic layers or carbon chains.^[31–33] The I_D/I_G ratio is 1.66 , indicative of a high proportion of defects, which is natural, considering the strong alkali (KOH) treatment utilized for activating carbon. The overtones of these fundamental vibrations, i.e., the 2D and the 2G modes are observed as a broad doublet at 2647 and 2966 cm^{-1} . As expected, the ZnV_2O_4 @TC composite exhibits contributions from both the oxide and the carbon, with the oxide's lattice vibrational modes (involving the V–O and Zn–O bonds) producing the bands in the 200 – 1000 cm^{-1} wave-number regime, and the TC gives rise to the D, G, 2D and 2G bands over the 1000 – 3200 cm^{-1} , with the I_D/I_G ratio being 1.36 .

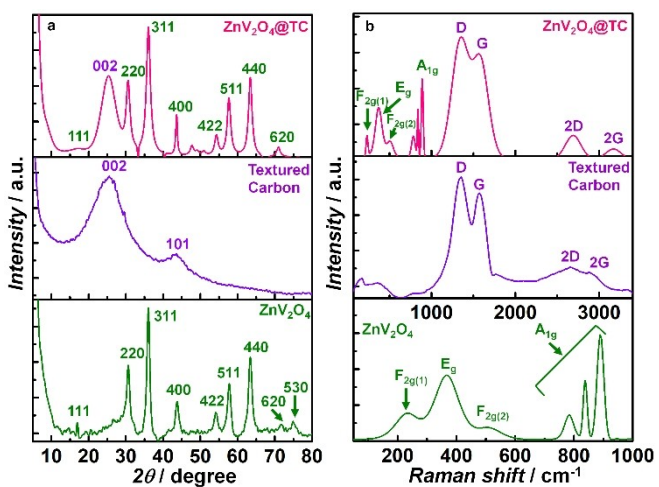


Figure 2. a) XRD patterns and b) Raman spectra of ZnV₂O₄, TC and ZnV₂O₄@TC composite.

Some of the vibrational modes of the oxide are slightly shifted relative to pristine ZVO, plausibly due to small variations induced in the V–O or Zn–O bond strengths, in the presence of the vicinal textured carbon.

BET study of TC was performed to determine its effective surface area; the plots are shown in the supporting information (Figure S1). The surface area and the average pore diameter are $\sim 841\text{ m}^2\text{ g}^{-1}$ and $\sim 2.2\text{ nm}$, respectively. The high surface area assists in improving the rate performance of the ZVO@TC composite compared to ZVO alone. Pore size distribution was also analyzed by the Horvath-Kawazoe method for TC and pores of dimensions less than 1 nm (micro-pores) are also found to be present and they are beneficial for adsorption of Zn(II) ions and electrolyte permeation.

Compositional aspects of the ZnV₂O₄@TC composite

XPS survey and core level spectra of the ZnV₂O₄@TC composite are shown in Figure 3. Survey spectrum in Figure 3(a) reveals distinct peaks due to the following core-levels: V3p, Zn3p, Zn3s, C1s, V2p, O1s, V2s and Zn2p and these originate from ZnV₂O₄ and TC. The Zn2p spectrum (Figure 3b) shows two intense sharp peaks due to the spin-orbital split at 1021.5 and 1044.6 eV corresponding to the Zn2p_{3/2} and Zn2p_{1/2} components, with an intensity ratio of ~ 2.4 . The raw V2p spectrum (Figure 3c) comprises of twin peaks due to the spin-orbital split (V2p_{3/2} and V2p_{1/2}), and these are further sub-divided into peaks at 516.6 and 523.8 eV from the V⁴⁺ state, and 517.2 and 524.6 eV from the V⁵⁺ state, with contributions of 61.8% and 38.2% for V(IV) and V(V) respectively. The existence of different valent states for vanadium indicates that the material has multiple redox sites, favorable for ion-adsorption and the subsequent Faradaic charge transfer and reaction. The spectrum broadly resembles that reported previously for ZnV₂O₄ nanowires, prepared using a hydrothermal route, and the V⁵⁺ assignments are based on their report.^[27] The asymmetric C1s spectrum (Figure 3d), is deconvoluted into three peaks at 284.2, 285.0 and 288.2 eV with percentage contributions of 44.40%, 34.83% and 20.76%, which are attributed to the C–C, C–O and the π – π^* satellite. As seen earlier from XRD and Raman data, TC is composed of a graphitic network with oxygen functionalities attached to the carbons. This is re-affirmed from the strong C–O signal observed here, which is largely due to the –COOH and –C–OH groups, typically located at the edges of the hexagonal graphitic 2D-layers. The broad O1s signal (Figure 3e) is deconvoluted into three components at 530.0, 531.4 and 533.2 eV, which are associated with the Zn–O or V–O bonds, C–O groups and the adsorbed water molecules respectively. The elemental composition histogram is shown in

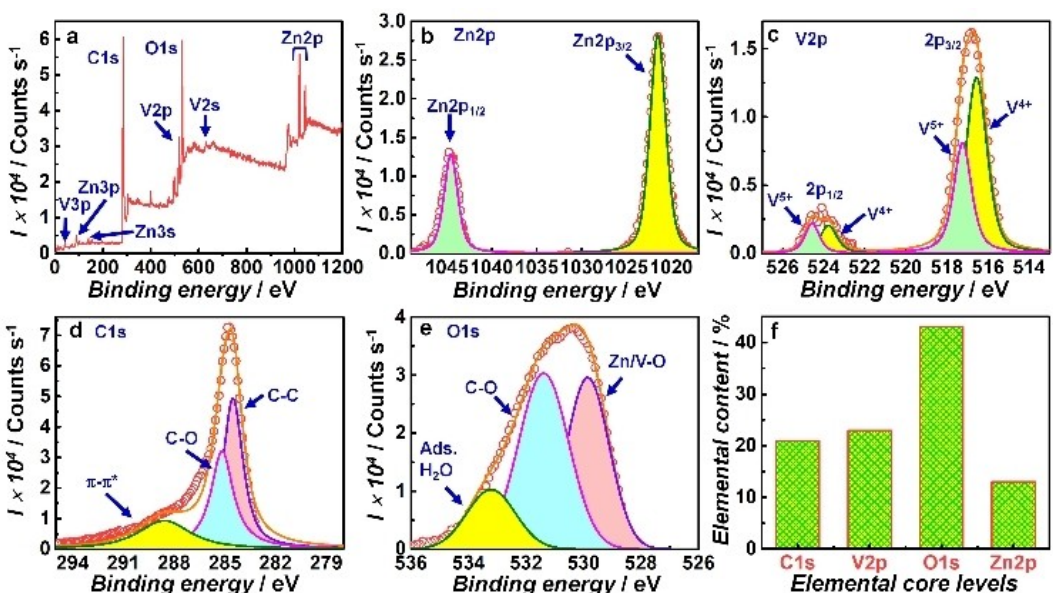


Figure 3. a) survey spectrum, core level spectra of b) Zn2p, c) V2p, d) C1s and e) O1s, and f) elemental composition histogram of the ZnV₂O₄@TC composite.

Figure 3(f), which shows that Zn, V, O and C are present at 13%, 23%, 43% and 21% contents respectively. The ratio of V:Zn stands at 1.76, which is close to the expected stoichiometry of 2:1, as in ZnV_2O_4 .

Electrical conduction behavior of cathode materials

The dc electrical conductivities (σ) of the cathode materials, were estimated from their current-voltage (I - V) plots (Figure 4a) recorded in a sandwich architecture of SS/sample/SS (SS is stainless steel), over the -1 to $+1$ V voltage range. TC exhibits a sigmoidal I - V profile. Over the short regime where the dependence is linear, a conductivity of $3.65 \times 10^{-4} \text{ S cm}^{-1}$ is calculated from the expression:

$$\sigma = \left(\frac{1}{R} \right) \times \left(\frac{d}{a} \right),$$

where $1/R$ is the slope, d is the sample thickness, and a is the cross-sectional area. Conduction in TC stems from the graphitic carbon network, where carbons are arranged in a hexagonal lattice, with three sp^2 -carbons forming σ -bonds in-plane. The fourth unhybridized (π)-electron moves freely above and below the plane, thereby imparting high conductivity to the material. The conductivity of pristine ZnV_2O_4 is $2.7 \times 10^{-7} \text{ S cm}^{-1}$, which is approximately 10^3 times lower than that of pure TC. The mixing of ZnV_2O_4 and TC will result in a substantially improved

conductivity for the composite compared to the pristine oxide, which serves two purposes: 1) The rate performance increases, due to faster electron transport across the cross-section of the material relative to ZVO. It must be noted that during discharge, for every electron injected into the material (under the applied electric field), a charge compensating cation will be accommodated in the material, thereby also ensuring that ion-storage is enhanced. 2) TC also assists in buffering the volume expansion experienced by the ZVO lattice during $\text{Zn}^{(\text{II})}$ ion insertion by relieving the mechanical strain. It acts as a cushion and prevents structural collapse. This is further evidenced from the XRD results of the post-cycled $\text{ZnV}_2\text{O}_4@\text{TC}$ composite shown in the latter part. In absolute terms, in spite of not being as high as that of TC, the reason for the moderate conductivity of pristine ZnV_2O_4 is the presence of mixed valent states of vanadium ($\text{V}^{3+}/\text{V}^{5+}$). Inter-valent charge transfer between two vicinal vanadium ions in two different oxidation states, imparts the observed conductivity. $\text{ZnV}_2\text{O}_4@\text{TC}$ composite has an electrical conductivity value of $1.4 \times 10^{-4} \text{ S cm}^{-1}$ which is three-orders of magnitude higher than that of pristine ZVO, thus rendering it to be suitable for battery applications.

Electrochemical characteristics of ZIBs

The electrochemical charge-discharge properties (CV and GCD plots, over 0.2 to 1.8 V, versus Zn^{2+}/Zn) of ZIBs, with the following cathodes: pristine ZnV_2O_4 , $\text{ZnV}_2\text{O}_4@\text{TC}$ composite and

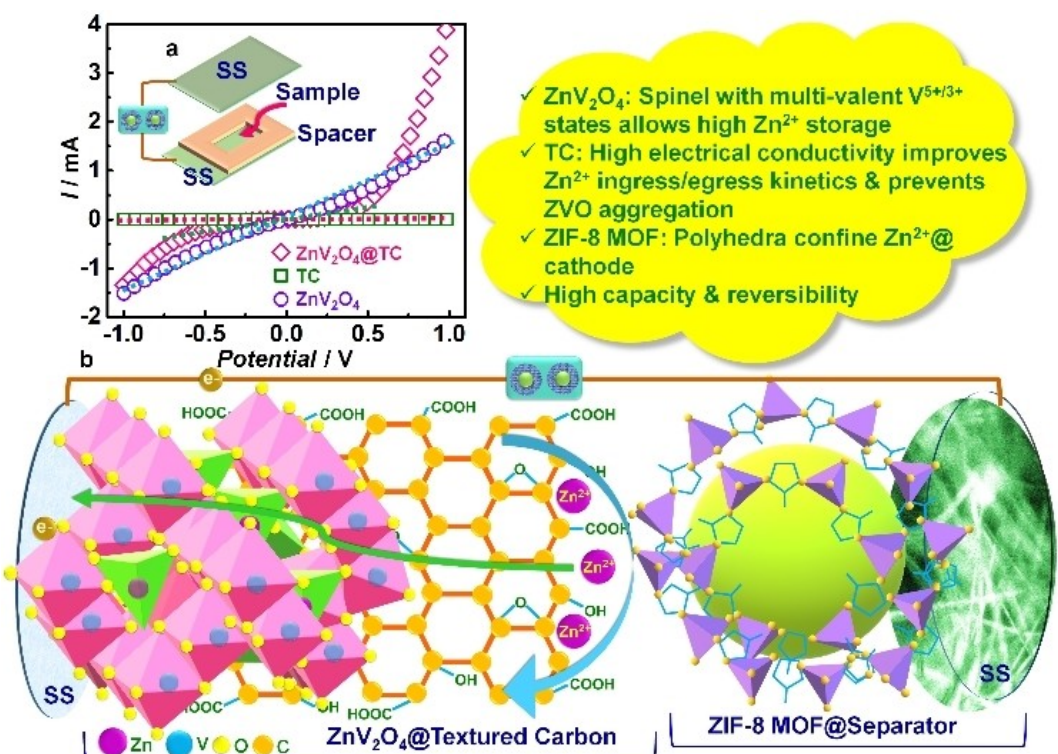


Figure 4. a) I - V characteristics of the ZnV_2O_4 nanorods, TC and their (3:1) composite, inset of a) is the cell configuration employed for the measurements; the dotted lines represent the linear fits. b) Schematic illustration of charging and discharging of a SS/ $\text{ZnV}_2\text{O}_4/\text{TC}$ (3:1)-ZIF-8@separator/Zn cell with a $\text{Zn}(\text{CF}_3\text{SO}_3)_2$ /acetonitrile electrolyte.

$\text{ZnV}_2\text{O}_4@\text{TC}/\text{ZIF-8}@{\text{separator}}$ are shown in Figures 5 and 6. The anode was Zn, and the non-aqueous electrolyte was 0.5 M $\text{Zn}_2(\text{CF}_3\text{SO}_3)_2$ dissolved in acetonitrile. The CV plots recorded at 0.1 mVs^{-1} , in the first cycle (Figure 5a–c) are characterized by the principal redox couples ($E_{\text{red}}/E_{\text{ox}}$) at 1.03/1.45 V, 0.94/1.29 V and 0.94/1.06 V. The Zn(II) ion ingress-egress reactions are expressed in equations below.



It was clearly observed that the $\text{ZnV}_2\text{O}_4@\text{TC}$ composite shows a trend to be oxidized at a lower voltage due to more carbon content hence more electrical conductivity. Post hundred charge-discharge cycles, the peak anodic/cathodic currents decrease for the pristine ZVO and the ZVO@TC composite based cells, whereas they remain almost unchanged for the cell which contains the ZIF-8@separator layer. The ZIF-8 MOF layer in contact with the ZVO@TC cathode reduces the capacity fade with cycling, for it prevents the Zn^{2+} loss during discharge, by confining the Zn(II) ions at the cathode, thus maximizing ion-storage, and also enhancing the reversibility. CV plots recorded at higher scan rates (Figure 5a'–c') in the range of $1\text{--}10 \text{ mVs}^{-1}$, show that the ZIBs are fairly reversible at

these rates as well, particularly the one with the ZIF-8@separator. The CV plots show that the anodic/cathodic peak current densities are nearly the same, suggestive of similar quanta of Faradaic mass transfer in the oxidation and reduction half-cycles. The ability of these cathodes to be able to maintain good reversibility at high scan rates again supports a good rate response.

To estimate the diffusive and capacitive components separately, the following equations were used for the $\text{ZnV}_2\text{O}_4@\text{TC}/\text{ZIF-8}@{\text{separator}}$ based ZIB.

$$i(\nu) = a\nu^b \quad (3)$$

$$\log(i(\nu)) = \log(a) + b \log(\nu) \quad (4)$$

In Equations (3) and (4), a and b are adjustable parameters, ν and $i()$ are the scan rate and the peak current at a particular scan rate. From the slope of the $\log(i(\nu))$ versus $\log(\nu)$ plot (Figure 5d), "b" was calculated. The magnitude of "b" helps in understanding the kinetic mechanism of the electrochemical charge storage in the ZIB. When "b" is 1, then the process is non-Faradaic via electrical double layer formation and when "b" is 0.5, then charge storage occurs through Faradaic-diffusion controlled redox reactions. Therefore, a value in-between 0.5 and 1 implies a charge storage process that combines the two

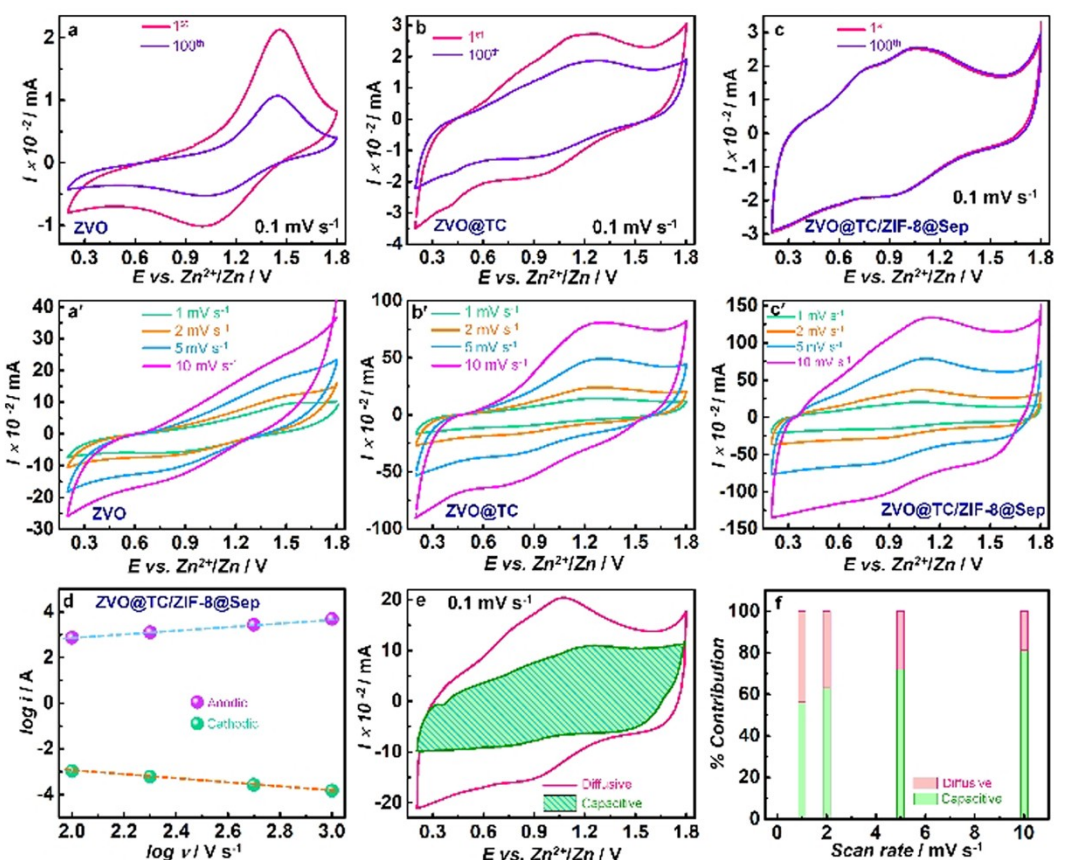


Figure 5. CV plots of ZIBs with Zn anode and the following cathodes: ZnV_2O_4 , $\text{ZnV}_2\text{O}_4@\text{TC}$ and $\text{ZnV}_2\text{O}_4@\text{TC}/\text{ZIF-8}@{\text{Separator}}$: (a–c) at 0.1 mVs^{-1} , after 1st and 100th cycle and (a'–c') at different scan rates ranging from 1 to 10 mVs^{-1} . For a $\text{ZnV}_2\text{O}_4@\text{TC}/\text{ZIF-8}@{\text{Separator}}$ based ZIB: (d) $\log i$ versus $\log \nu$ plot, (e) representative cyclic voltammograms illustrating the capacitive and diffusion contributions and (f) %contributions of diffusion and capacitive components.

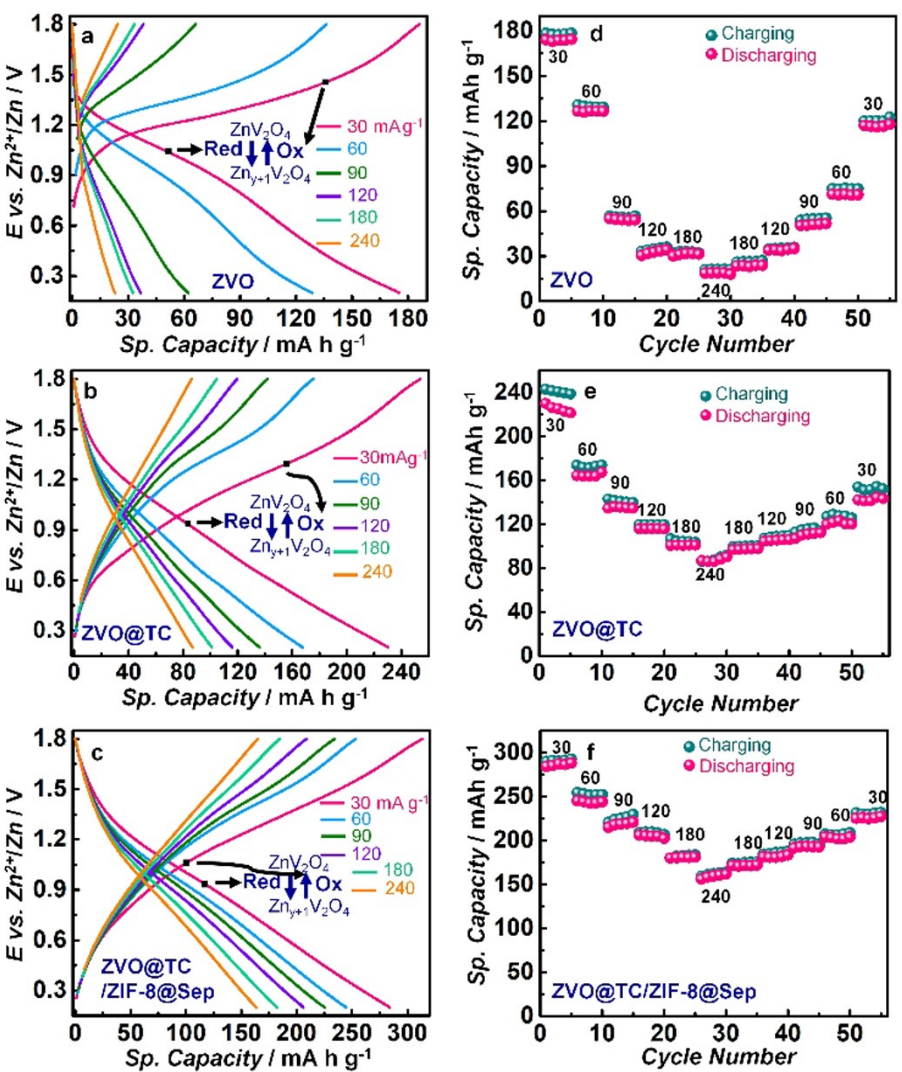


Figure 6. ZIBs with Zn anode and the following cathodes: ZnV_2O_4 , $\text{ZnV}_2\text{O}_4@\text{TC}$ and $\text{ZnV}_2\text{O}_4@\text{TC}/\text{ZIF}-8@\text{Sep}$: a–c) GCD plots at different current densities and d–f) rate capability curves, as a function of cycling and current densities.

mechanisms of i) the build-up of ionic charge on its' surface which is directly proportional to the applied potential, and ii) mass-transfer by electron or ion intercalation and deintercalation. The closer b is, to 0.5 or 1 determines the primary mechanism. Battery-type materials exhibit a lower b compared to capacitive materials. The value of b here is 0.8. The large value of b is indicative of a dominant EDL formation for charge storage. The triangular nature of the GCD plots also reaffirm this. To quantify the capacitive and diffusion based components, the following equations were used. When a material or cell undergoes non-Faradaic charge accumulation/release, the current varies linearly with scan rate and for a diffusion-controlled process, the current is directly proportional to the square root of scan rate.

$$i(V) = i_{\text{cap}} + i_{\text{diff}} = k_1 \nu + k_2 \nu^{1/2} \quad (5)$$

or

$$i(V)/\nu^{1/2} = k_1 \nu^{1/2} + k_2 \quad (6)$$

In Equation (5), i_{cap} and i_{diff} are the capacitive- and diffusion-currents respectively. The constants k_1 and k_2 are determined from the slopes and the intercept of a linear plot of $i(V)/\nu^{1/2}$ versus ν by using Equation (6). Figure 5(e) is a representative cyclic voltammogram wherein the shaded area in the CV curve ensconces the capacitive contribution, which is 56%, and the diffusive contribution is 44% (Figure 5f). Here in the non-aqueous system, the dominant capacitive behavior is responsible for the good rate response and cycle life.

In the GCD plots obtained at different current densities for ZVO (Figure 6), discharge and charge plateaus were observed at ~ 1.0 V and ~ 1.4 V which agree well with the corresponding CV curves. Highest charge and discharge capacities were ~ 185 and ~ 175 mAh g⁻¹ at 30 mA g⁻¹ which reduced drastically to ~ 24 and ~ 23 mAh g⁻¹ at 240 mA g⁻¹. These lower values attained at high current densities are mainly due to the low

conductivity of pristine ZVO, hence lower active material utilization. Rate capability curve also shows that the cell retains only $\sim 65\%$ of its highest discharge capacity when tested at 30 mA g^{-1} after 200 cycles of the initial run. The loss in capacity with cycling is due to the volume expansion and contraction experienced by ZVO, during Zn^{2+} intercalation and deintercalation. This repetitive process causes volume strain leading to structural instability and collapse, followed by pulverization and detachment of the active material from the current collector. The net outcome is loss in capacity, which is seen here. In contrast, the $\text{ZnV}_2\text{O}_4@\text{TC}$ (60:20) composite shows better performance in terms of capacity and cycling stability. The highest discharge capacity was $\sim 230 \text{ mAh g}^{-1}$ at 30 mA g^{-1} and $\sim 38\%$ was retained at 240 mA g^{-1} . But after 200 cycles, 67% of the initial fresh cells' highest capacity was retained. This improvement in the cell performance is mainly due to following points: a) Addition of TC increases the conductivity of the cathode, and this directly controls the kinetics of the Faradaic reactions. b) Unlike pristine ZVO which comprises of aggregated nanoparticles, and is unable to buffer the volume changes of the material during Zn^{2+} ingress/egress, TC can accommodate the volume variation to some extent, for the TC is endowed with nanoscale porosity, and this free space is therefore available for the ZVO lattice to expand into. Furthermore, pristine oxide particles have a strong tendency to agglomerate, thus blocking many electrochemically active sites from electrolyte ion-penetrations and resulting in a lowered capacity. The inclusion of TC not only limits the aggregation of ZVO particles, but they also serve as electrically conducting interconnects, thus, increasing ion-storage capacity. Optimized composition ratio is also an important factor for achieving optimum conductivity and active material content in case of the cathode. This is supported by the GCD, cycling stability and CE plots of $\text{ZnV}_2\text{O}_4@\text{TC}$ (70:10) (Figure S2) where the performance of the cell is lower in comparison to the $\text{ZnV}_2\text{O}_4@\text{TC}$ (60:20) composition ratio.

For the composite based cell: $\text{ZnV}_2\text{O}_4@\text{TC}/\text{Zn}$, the charge-discharge plateaus of the oxide are not well-resolved, possibly due to the carbon content. The cell was further modified by introducing a thin layer of ZIF-8 MOF on the separator side facing the cathode as it was realized that the $\text{ZnV}_2\text{O}_4@\text{TC}/\text{Zn}$ cell was still deprived of attaining the maximum capacity value with the TC additive. Highest charge and discharge capacities of ~ 313 and $\sim 283 \text{ mAh g}^{-1}$ are achieved respectively at 30 mA g^{-1} in the $\text{ZnV}_2\text{O}_4@\text{TC}/\text{ZIF-8}@\text{separator}/\text{Zn}_2(\text{CF}_3\text{SO}_3)_2$ -acetonitrile/Zn cell. At 240 mA g^{-1} , charge and discharge capacities of ~ 165 and $\sim 163 \text{ mAh g}^{-1}$ were obtained. After cycling the cell for 200 cycles, nearly 80% of fresh cells' highest capacity was retained in rate capability. This is a remarkable achievement, for even after increasing the current density by eight-fold times, a large capacity is retained by the ZIB. During the discharge process, when $\text{Zn}(\text{II})$ ions intercalate into the cathode, the ZIF-8 MOF layer serves as a physical barrier and restrict the undesirable Zn -ion back diffusion into the electrolyte, restraining them at the cathode, and maximizing the capacity. The back diffusion is always there due to the concentration gradient or back emf which inhibits the cell from

achieving the highest possible capacity. During the charging process, while the applied electric current drives the migration of $\text{Zn}(\text{II})$ ions from the cathode to the anode, the ZIF-8 layer, now allows their diffusion through the ZIF-8 MOF lattice. The MOF structure has open channels and hence permits the ion-movement. The schematic in Figure 4b shows the structure of the MOF, and the roles of the various components in realizing the high cyclability and good capacity for this cell. GCD plots for all three different cells at a particular current density (30 mA g^{-1}) are provided in the supporting information (Figure S3). A comparison of capacities with reported non-aqueous ZIBs is provided in Table 1. Our values are superior to reported values, thus justifying the use of the double layered Zn based cathode.

CV, GCD, cycling stability, Coulombic efficiency and rate capability plots of ZIB with the following configuration: SS-TC/ $\text{Zn}(\text{CF}_3\text{SO}_3)_2$ in AN/Zn, and are shown in supporting information (Figure S4). In this cell, TC, carbon black and PVDF were mixed in the 80:10:10 weight ratio and used as the cathode, and Zn was employed as the anode. The plots (Figure S4) reveal that the ZIB gave an initial capacity of $\sim 40 \text{ mAh g}^{-1}$ at 30 mA g^{-1} current density. A rectangular CV curve is obtained with a slight hump at 0.89 and 1.06 V during reduction and oxidation respectively which indicated the slight pseudo-capacitive behavior of carbon possibly due to some reactions of the attached functional groups. Carbon contributes to the overall capacity of the ZVO@TC based ZIBs and it largely stores charge via EDL formation. A schematic diagram illustrating how TC stores and releases charge is shown in Scheme S1 (Supporting Information). During discharging, the $\text{Zn}(\text{II})$ ions are adsorbed on carbon, via electrostatic interactions between the oxygens on the polar $-\text{OH}$, $\text{C}-\text{O}-\text{C}$ and $-\text{COOH}$ groups, and during charging, the CF_3SO_3^- electrostatically bind to the positively charged graphitic backbone. Coulombic efficiency is found to lie in the range of 94–99% with nearly $\sim 100\%$ capacity retention after 100 cycles. This is also supported by the CV curve in the 100th cycle as there was no noticeable change in pattern of the curve indicating no structural changes occurred in the carbon. While TC does contribute to the overall capacitance of the ZVO@TC cathode, but the major contribution originates from the mixed metal oxide.

Cycling stability (at 30 mA g^{-1}) and Coulombic efficiency plots show (Figure 7a–c) only $\sim 45\%$ of initial capacity retention for pristine ZVO which is due to the aforementioned issue of volume variation. For $\text{ZnV}_2\text{O}_4@\text{TC}$ cell, capacity retention was elevated to $\sim 85\%$ and for the cell with the ZIF-8@separator, $\sim 91\%$ of the initial capacity was retained, for $\text{Zn}(\text{II})$ ions are effectively confined to the cathode. Coulombic efficiency in these cases are in between 93–98%, which supports the fact of good $\text{Zn}(\text{II})$ -ion ingress-egress reversibility.

Nyquist plots of ZIBs with pristine ZnV_2O_4 , $\text{ZnV}_2\text{O}_4@\text{TC}$ composite and $\text{ZnV}_2\text{O}_4@\text{TC}/\text{ZIF-8}@@\text{separator}$ as cathodes before and after cycling are shown in Figure 7(d–f). The plots were fitted into a $[R_s(R_{ct}C_{dl})Z_W]$ circuit. Charge transfer resistance is the largest for pristine ZVO cell, and least for the one with the composite and the ZIF-8@separator. Diffusional conductance is

Table 1. Comparison of this work with literature reports on non-aqueous ZIBs.

Cathode material	Voltage window [V]	Discharge capacity [mA h g ⁻¹]/Cycling performance	Electrolyte	References
K _{1.6} Mn _{1.2} Fe(CN) ₆	0.7–1.9	65.5 (200 mA g ⁻¹) 94% capacity retention after 8500 cycles	2 M Zn(ClO ₄) ₂ in tetraethylene glycol dimethyl ether	[39]
Na ₃ V ₂ (PO ₄) ₃	0.6–1.8	85 (500 mA g ⁻¹) 100% Capacity retention after 600 cycles	1 M NaCF ₃ SO ₄ + 0.1 M Zn(CF ₃ SO ₃) ₂ in triethyl phosphate (TEP)	[40]
Graphite	0.7–2.7	105 (100 mA g ⁻¹) 97.5% capacity retention after 2000 cycles	0.2 M (Zn(CF ₃ SO ₃) ₂) in propylene carbonate (PC)/dimethylsulfoxide (DMSO) (1:4)	[41]
δ-MnO ₂	0.05–1.9	123 (12.3 mA g ⁻¹) 44.7% capacity retention (125 cycles)	0.5 M Zn(TFSI) ₂ electrolyte in AN	[42]
γ-MnO ₂	1–1.8	146.2 (15 mA g ⁻¹) 90% capacity retention after 100 cycles	Poly(ethylene oxide) – (Zn(CF ₃ SO ₃) ₂) -Branched Aramid Nano-Fibers (PZB) Composite	[43]
V ₂ O ₅ ·H ₂ O	0.5–1.8	70–175 at 5 mA g ⁻¹ from 1 st to 50 th cycle	0.25 M Zn(CF ₃ SO ₃) ₂ in AN	[22]
Co(III)-rich Co ₃ O ₄ /CFC	0.8–2.3	178.6 (0.5 A g ⁻¹) 94.6% capacity retention (2000 cycles at 2 A g ⁻¹)	PAM/2 M ZnSO ₄ / 0.1 M CoSO ₄	[44]
ZnNi _x Mn _x Co _{2-2x} O ₄ (x = 1/2)	0.9–2.15	180 (21 mA g ⁻¹) 93% capacity retention after 200 cycles	0.3 M Zn(OTf) ₂ + 200 ppm DABCO in MeCN	[45]
V ₂ O ₅ /graphite	0.2–1.8	212 (2 A g ⁻¹) after 200 cycles (~85% retention)	Gelatine /alginate based membrane electrolyte	[46]
ZnV ₂ O ₄ /TC (3:1) composite-ZIF-8@separator (This Work)	0.2–1.8	283 (30 mA g ⁻¹) 91% capacity retention after 200 cycles	0.5 M Zn(CF ₃ SO ₃) ₂ in AN.	

the largest for the cell with the separator, indicating the MOF helps with rapid diffusion of Zn-ions as well.

For pristine ZVO, the plots show a large, depressed semi-circle, followed by an almost flattened line parallel to the x-axis whereas the plots for the composite based cells with and without the MOF show a skewed semi-circle, followed by an inclined line. The ZVO plots were fitted into a $[R_s(R_{ct}C_{dl})(R_{gb}C_{gb})Z_w]$ circuit. R_s is the solution resistance (of the Zn₂(CF₃SO₃)₂/AN electrolyte), the electrical double layer capacitance, and the charge transfer resistance at the cathode/electrolyte interface produce C_{dl} and R_{ct} and the Warburg impedance gives Z_w . ZVO is composed of a large number of juxtaposed nanocrystallites (evidenced from the TEM studies), and due to the low electrical conductivity of pure ZVO, the grain boundaries (gb) in ZVO give rise to the R_{gb} and C_{gb} . In the ZnV₂O₄@TC (3:1) composite, the presence of homogeneously distributed electrically conducting TC conduits, effectively lowers the intra-particle resistance, and eliminates the resistive parameters associated with the grain boundaries.

To begin with the solution resistance is in the range of 2–6 Ω cm² for all cells, and is independent of the cathode, as expected. R_{ct} is the highest for the ZVO/electrolyte interface, compared to the remaining two cathode architectures, due to the poor electrical conductivity of the pure ZVO, thus restricting the number of ions that can crossover to the electrode, and reducing the capacity. The R_{gb} is 5487.3 Ω cm², and this resistance inhibits the unhindered diffusion of Zinc-ions across the cross-section of ZVO. From the Warburg parameter, Y_o , the diffusion coefficient (D) of Zn(II) ions was calculated using the following Equations (7) and (8). 'σ' has been calculated from Equation (8).

$$\sigma = \frac{RT}{\sqrt{2} n^2 F^2} \left[\frac{2}{C\sqrt{D}} \right] \quad (7)$$

$$\sigma = \frac{1}{\sqrt{2} Y_o} \quad (8)$$

Here, $R = 8.314 \text{ J K}^{-1} \text{ mol}^{-1}$, $T = 298 \text{ K}$, $n = 2$, $F = 96500 \text{ C mol}^{-1}$ and $C = \text{concentration of Zn}_2(\text{CF}_3\text{SO}_3)_2 \text{ electrolyte in mol cm}^{-3}$ and D was estimated to be of the order of $10^{-15} \text{ cm}^2 \text{ s}^{-1}$ which is considerably low due the aforementioned reasons. The impedance data of the composite based cells with and without the Zn-MOF layer were fitted into a $[R_s(R_{ct}C_{dl})Z_w]$ circuit. For the ZnV₂O₄@TC (3:1) composite and ZnV₂O₄@TC/ZIF-8@separator-based cells, D was observed to be 10^3 times higher implying the resistance offered by the grain boundaries in ZVO are overcome by the inclusion of conductive TC and in addition the Zn-MOF layer also facilitates diffusion due to its open channeled structure. In the cell with the ZIF-8@separator, R_{ct} decreases by significantly in post 200 cycles. That also is quite natural and reported before due the electro-activation^[23,34] of the active materials and electrochemical polishing of the electrode surface and hence increasing reversibility of the cell. All the EIS parameters are presented in Table 2.

Critical role of ZIF-8 MOF in controlling ZIB performance

The role of the ZIF-8- MOF in ameliorating the ZIB performance was analyzed in detail. XRD pattern of ZIF-8 MOF in Figure 8(a) shows a multitude of intense peaks at $2\theta = 7.3^\circ, 10.35^\circ, 12.66^\circ, 14.77^\circ, 16.38^\circ, 18.02^\circ, 22.17^\circ, 24.82^\circ, 26.53^\circ, 28.1^\circ, 30.6^\circ, 30.6^\circ, 34.1^\circ$ are attributed to (011), (002), (112), (022), (013), (222),

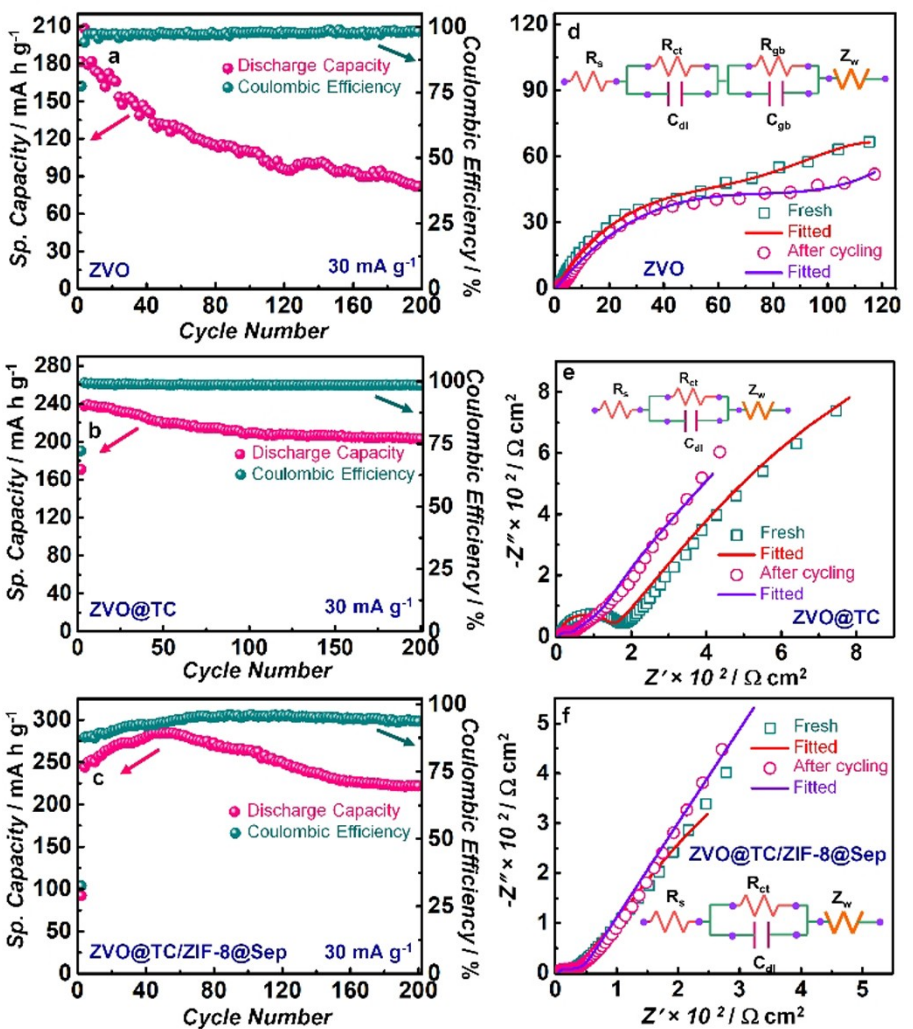


Figure 7. ZIBs with Zn anode and the following cathodes: ZnV_2O_4 , $\text{ZnV}_2\text{O}_4@\text{TC}$ and $\text{ZnV}_2\text{O}_4@\text{TC}/\text{ZIF-8}@\text{Sep}$: a–c) variation in specific capacity and Coulombic efficiency as a function of number of cycles at 30 mA g^{-1} ; d–f) Nyquist plots for the same ZIBs, before cycling, and after 200 charge-discharge cycles, recorded over a frequency range of 1 MHz to 0.01 Hz, under the open circuit potential, and an ac amplitude of 20 mV. Inset of d) is the equivalent circuit used for fitting the data.

(114), (233), (224), (134), (044), (244) and (235) planes of the cubic crystal structure, in accordance with JCPDS 00-062-1030. The pattern reflects the phase purity of the MOF. In ZIF-8, the Zn-atoms are covalently linked to the nitrogens via the organic linkers: 2-methylimidazolium ions, resulting in a nanoporous arrangement encompassing multi-membered-rings of Zn_4N tetrahedral clusters. These open channels are ideal for ion diffusion, and its well-established chemically and thermally stable structure^[35] are additional advantages, further supporting its use as the overlayer for maximizing cyclability and storage response. The structure concurs with the reported structure for ZIF-8 MOF in various reports.^[36,37] The FE-SEM images (Figure 8b, c) show irregular shaped particles with sizes ranging from 2 to 4 μm . TEM images (Figure 8d, e) show distorted polyhedral shapes for the MOF and these are overlapping and fused with each other. The SAED pattern shows concentric rings, and they are indexed to the (011) and the (222) planes. To determine the ability of the ZIF-8 MOF to allow the transport

of Zn(II) ions through its matrix, the CV plots of a film of ZIF-8 deposited over FTO were recorded at different scan rates in a three-electrode configuration, with Ag/AgCl/KCl as the reference, and a Pt rod as the CE (Figure 8f). The CV plots show a well-defined set of $E_{\text{ox}}/E_{\text{red}}$ peaks at 0.38 and 0.26 V, and the peak current densities increase as function of scan rate. Albeit slight positional differences, these plots are similar to the reversible CV profiles obtained for ZIF-8 in an earlier report, in a KCl electrolyte modified with different redox mediators.^[38]

The anodic/cathodic peak current densities (i_{pa} or i_{pc}) were plotted as a function of square root of scan rate ($\nu^{1/2}$) as displayed in Figure 8(g) and the diffusion coefficient (D) for Zn(II) ions was estimated from the Randles-Sevcik equation.

$$i_{\text{pa}} \text{ or } i_{\text{pc}} (\text{A cm}^{-2}) = (2.67 \times 10^5) \times n^{3/2} \times C_o \times D^{1/2} \times \nu^{1/2} \quad (9)$$

In Equation (9), C_o is the concentration of $\text{Zn}_2(\text{CF}_3\text{SO}_3)_2$ electrolyte in mol cm^{-3} and n is the number of electrons

Table 2. EIS fitted parameters for fresh and cycled ZIBs.

Cell configuration	R_s [Ωcm^2]	R_{ct} [Ωcm^2]	C_{dl} [Fcm^{-2}]	R_{gb} [Ωcm^2]	C_{gb} [Fcm^{-2}]	Y_o [$\text{mSs}^{1/2} \text{cm}^{-2}$]
Pristine ZnV_2O_4 (Fresh)	2.6	785.5	587.14	5487.3	959.4	0.20
Pristine ZnV_2O_4 (Cycled)	4.1	720.0	115.0	6042.6	779.7	0.22
$\text{ZnV}_2\text{O}_4/\text{TC}$ (3:1)//Zn (Fresh)	3.4	11.6	38.3	–	–	4.5
$\text{ZnV}_2\text{O}_4/\text{TC}$ (3:1)//Zn (Cycled)	2.7	22.3	30.1	–	–	6.3
$\text{ZnV}_2\text{O}_4/\text{TC}$ (3:1)-ZnHTC@Sep//Zn (Fresh)	3.5	196.5	20.1	–	–	7.6
$\text{ZnV}_2\text{O}_4/\text{TC}$ (3:1)-ZIF-8@Sep//Zn (Cycled)	5.4	44.6	9.4	–	–	10.4

involved in the redox reaction. From the slopes of the straight-line fits shown in Figure 8(g), the anodic and cathodic D-values were determined to be 1.47×10^{-10} and $1.32 \times 10^{-10} \text{ cm}^2 \text{ s}^{-1}$. These values are nearly the same, indicating that the rate of Zn(II) ion insertion is equal to the rate of Zn(II) ion extraction. It

reflects a good reversibility thus supporting the application of the ZIF-8 MOF layer in the cell.

This was supplemented by the cycling response achieved for the cell at 240 mA g^{-1} . Intermittently acquired GCD curves, during the long-term cycling for 500 charge-discharge cycles, are presented in Figure 8(h), and the variation in specific capacity and CE with cycling is shown in Figure 8(i). The initial capacity is 146 mAh g^{-1} (20th cycle), and it is 143 mAh g^{-1} , after 500 cycles; 98% capacity retention is registered for the $\text{ZnV}_2\text{O}_4/\text{TC-ZIF-8@separator/Zn}_2(\text{CF}_3\text{SO}_3)_2$ -acetonitrile/Zn cell, which demonstrates its outstanding endurance capability, particularly in view of the fact that it is difficult to achieve high storage and durability in non-aqueous ZIBs. Ex-situ images of the $\text{ZnV}_2\text{O}_4/\text{TC}$ electrodes before and after cycling are shown in Figure 9(a-d). As can be gauged from the images, prior to cycling, the ZVO particles and the TC are enmeshed together, and post-cycling some elongated particles are also observed, indicating the change in morphology induced by the repeated insertion and extraction of Zn(II) ions into and from the $\text{ZnV}_2\text{O}_4/\text{TC}$ matrix. The ex-situ XRD pattern for the cycled $\text{ZnV}_2\text{O}_4/\text{TC}$ electrode (Figure 9e) shows broadened peaks, with the principal Bragg's reflections still remaining, suggestive of the preservation of the polycrystallinity of the oxide and the carbon. Prominent peaks at $2\theta = 25.9^\circ, 36.0^\circ, 43.5^\circ, 54.3^\circ, 57.6^\circ$ and 63.3° are visible, and they stem from the (002) plane of graphite and the (311), (400), (422), (511) and (440) planes of ZVO with a fcc lattice. The optical microscopy images of the ZIF-8@separator, before and after cycling, are exhibited in

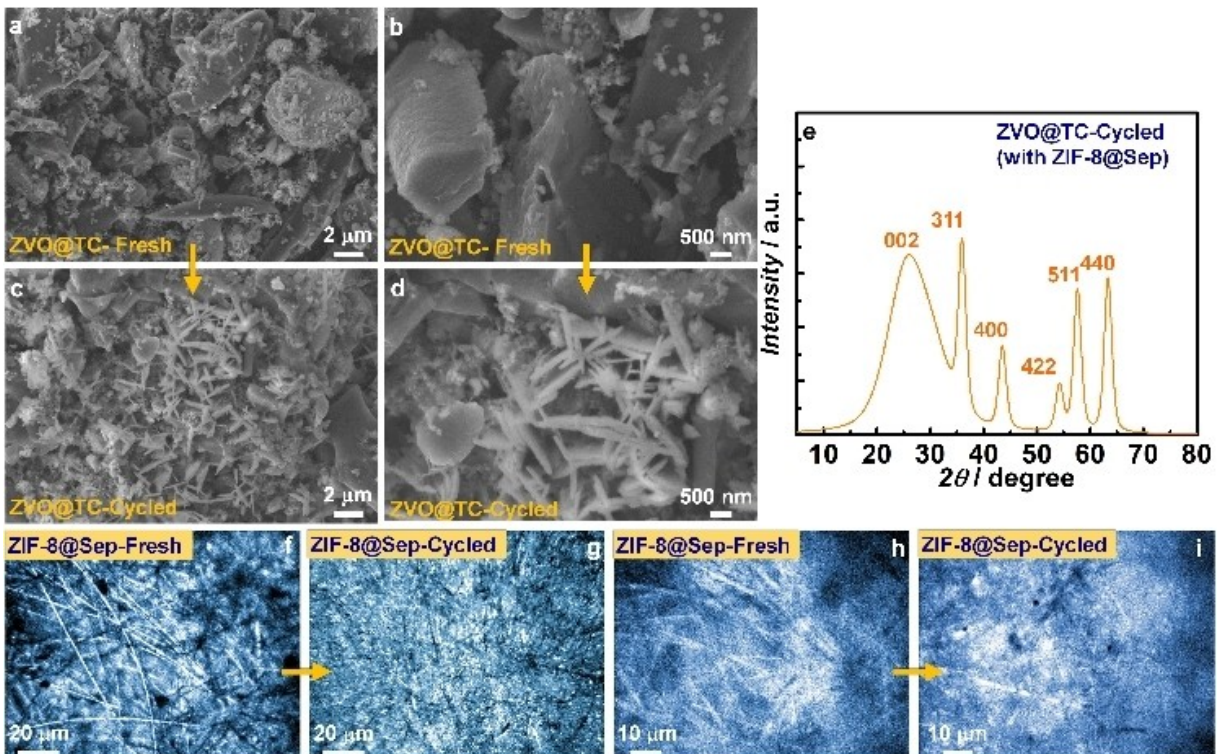


Figure 8. FE-SEM images of a, b) fresh and c, d) post-cycled (after 500 cycles) $\text{ZnV}_2\text{O}_4/\text{TC}$ electrodes encompassing CB and PVDF, extracted from the $\text{ZnV}_2\text{O}_4/\text{TC-ZIF-8@Sep-Zn}^{2+}/\text{Zn}$ battery, and e) its' ex-situ XRD pattern. Optical microscopy images of f, h) fresh ZIF-8@Separator and g, i) post-cycled (after 500 cycles) ZIF-8@Separator extracted from the $\text{ZnV}_2\text{O}_4/\text{TC-ZIF-8@Sep-Zn}^{2+}/\text{Zn}$ battery.

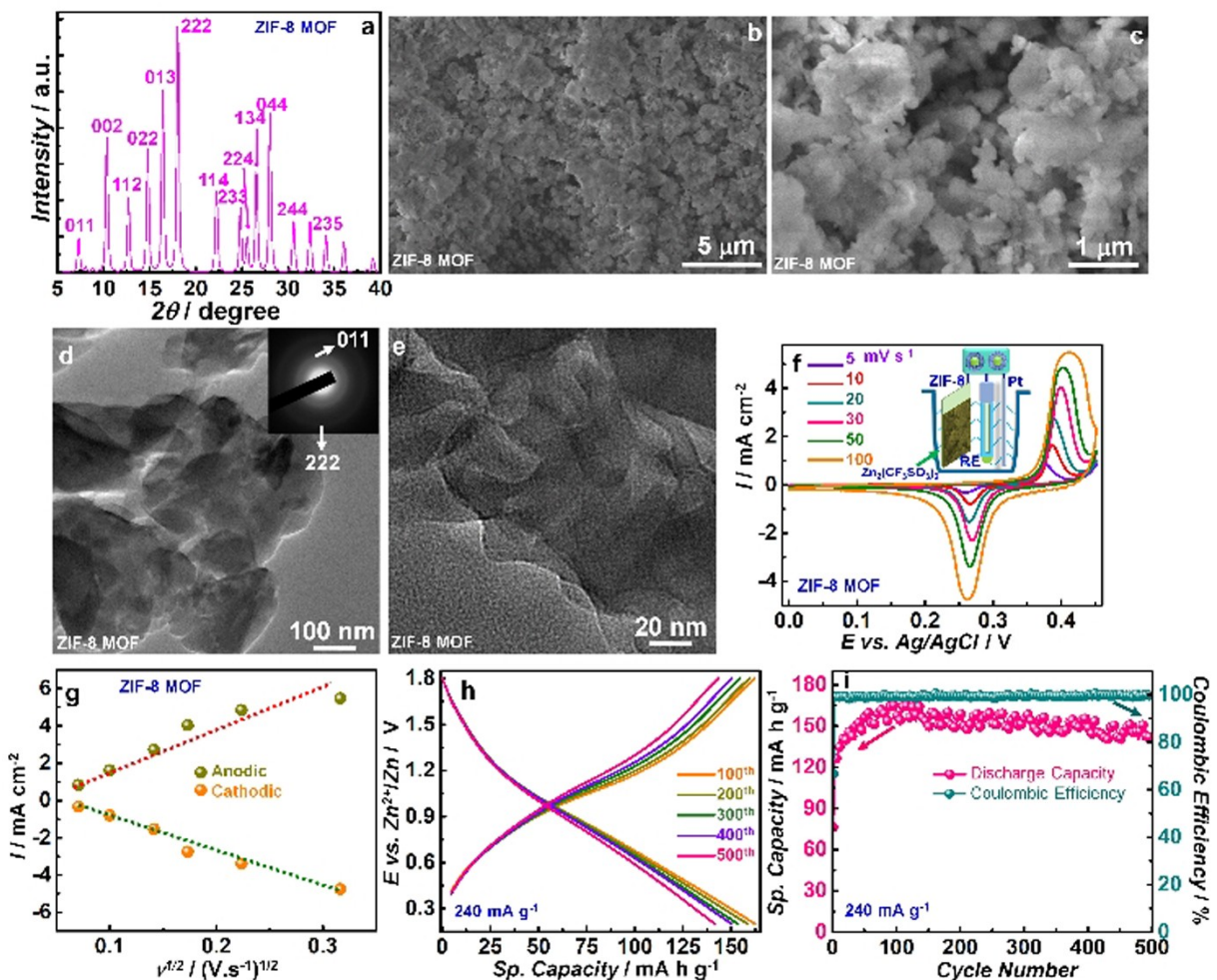


Figure 9. a) XRD pattern, b, c) FE-SEM images and d, e) TEM images of the ZIF-8-MOF; inset of d) is the corresponding SAED pattern. f) CV plots of a ZIF-8 MOF@FTO recorded in a three electrode cell, with Pt as the counter electrode, at different scan rates in a 0.5 M $\text{Zn}(\text{TC}_3\text{SO}_3)_2$ /acetonitrile electrolyte. g) peak anodic and cathodic currents versus square root of scan rate from f). h) GCD plots as a function of cycling, and variation in discharge capacity and CE versus number of cycles for a $\text{ZnV}_2\text{O}_4@\text{TC}/\text{ZIF-8}@\text{Sep-Zn}^{2+}/\text{Zn}$ battery.

Figure 9(f-i). The fresh assembly of the ZIF-8@separator, shows the mesh like network of the separator fibers to be coated with the MOF, and post-cycling the images are almost similar, notwithstanding, a small degree of fuzziness, and some loss in the image contrast. This again illustrates that the ZIF-8 MOF not only remains intact during cycling, but also contributes to enhancing the cyclability of the full cell, by indirectly assisting the cathode to maintain its structural integrity, by maximizing the Zn(II) ion uptake during discharge, by ensuring that charge reversibility is maintained with cycling, thus leading to the observed high discharge capacity over 500 cycles.

Furthermore, to show that ZIF-8 is not a major contributor to the cell's capacity, GCD and cycling stability plots of a ZIB with the cathode consisting of pristine ZIF-8 are shown in Figure S5 (Supporting Information). The capacity of pure ZIF-8 is found to be rather low ($\sim 18 \text{ mAh g}^{-1}$ at 30 mA g^{-1}) possibly due to the poor electrical conductivity of MOF. However, the $\text{ZnV}_2\text{O}_4@\text{TC}/\text{ZIF-8}@\text{separator}$ based ZIB that was developed in this work used a very small amount of ZIF-8 coating on the separator in terms of weight, i.e., 0.012 mg. So, the contribution

to overall capacity will be very less (0.144 mAh g^{-1}). In this cell, more than capacity, it is the structure of ZIF-8 which plays a crucial role in improving the capacity and the operational lifetime of the ZIB. The open porous structure with well-defined channels allows the facile diffusion of Zn(II) ions during charging and restrains them at the cathode during discharge.

Conclusion

By integrating a layer of a ZIF-8@separator in a non-aqueous ZIB with $\text{ZnV}_2\text{O}_4@\text{TC}$ as the cathode, a greatly enhanced Zn(II) ion storage performance was achieved compared to the cell with pristine ZVO or without the MOF layer. Firstly, the addition of TC to ZVO imparts the following benefits: 1) improved conductivity that facilitates electron transfer and transport across the active material, resulting in improved rate response, 2) provides a cushioning effect to relieve the strain experienced by ZVO by repeated Zn(II) ion ingress and egress, thus improving cycle life, and 3) restricts ZVO aggregation, thus

allowing ample contact with the electrolyte ions, and maximizing ion-uptake and hence capacity. The incorporation of the ZIF-8 MOF layer at the separator facing the $\text{ZnV}_2\text{O}_4@\text{TC}$ cathode, brings about a vast improvement in the ZIB performance, for the ZIF-8 layer prevents capacity fade with cycling, by efficiently confining the Zn(II) ions at the cathode during discharge, and affording fast ion diffusion through the open channels during charge endowing the cell with good reversibility. The ZIF-8 MOF layer also enjoys a high degree of crystallinity and chemical stability allowing it to remain unaffected by cycling, thus establishing its application to be a generic approach for improving the cycle life and capacity of ZIBs.

Experimental Section

Chemicals

Zinc acetate dihydrate ($\text{Zn}(\text{CH}_3\text{COO})_2 \cdot 2\text{H}_2\text{O}$, $\geq 99.0\%$), vanadium pentoxide (V_2O_5 , $\geq 99.0\%$), Zinc trifluoromethanesulfonate $\text{Zn}(\text{CF}_3\text{SO}_3)_2$, hydrazine hydrate (reagent grade, N_2H_4 50%–60%), zinc metal foil of 0.25 mm thickness, GF/D borosilicate glass fiber, Whatman filter paper were procured from Sigma-Aldrich and used as such. Carbon black (CB), poly(vinylidene fluoride) (PVDF, average M_w : 534000), N-methyl pyrrolidone (NMP), and sodium hydroxide (NaOH) were purchased from Merck. Ultrapure water (resistivity $\sim 18.2 \text{ M}\Omega \text{ cm}$) was obtained through a Millipore direct Q3UV system. Stainless steel (SS) foils were procured from Alfa Aesar. Betel nut shells were procured locally.

Synthesis of ZnV_2O_4 (ZVO) and textured carbon

ZnV_2O_4 was synthesized by a facile hydrothermal method based on a previous report. $\text{Zn}(\text{CH}_3\text{COO})_2 \cdot 2\text{H}_2\text{O}$ and V_2O_5 were taken in 30 mL of water in a 1:1 molar ratio. Hydrazine hydrate (1 mL) was added to the solution with vigorous stirring. Solution color turned into blue due to the conversion of V^{5+} to V^{4+} . The solution was then transferred into a Teflon lined autoclave and heated at 180°C for 15 h. It was cooled then at ambient temperature and the black colored solid was filtered and dried at 60°C in a hot air over for 12 h.

Textured carbon was synthesized from betel nut shells as a biomass source following a previous report. The shells were collected and washed several times with ultrapure water. The shells were cut into small pieces and transferred to an autoclave, heated at 70°C for 12 h to char the sample in the presence of ultrapure water. The resulting brown-reddish colored sample was washed with ethanol and dried at 70°C in open air. The dried sample was heated for 4 h to reach the final temperature of 750°C, and at this temperature, the heating was continued for another 4 h. The calcined carbon was ground and activated using aqueous KOH (1:1, w/w) using a minimum amount of water. The mixture was stirred at 80°C for 12 h. The mixture was filtered and washed with ultrapure water several times until the pH of the filtrate was 7. Finally, the textured carbon (TC) was dried at 70°C in open air and stored in a desiccator.

Synthesis of ZIF-8 metal-organic framework (MOF)

ZIF-8 was prepared by a simple co-precipitation method following a previous report. $\text{Zn}(\text{NO}_3)_2 \cdot 6\text{H}_2\text{O}$ (1 mmol, 297 mg) was dissolved

in 20 mL methanol to obtain solution-A, and methyl imidazole (8 mmol, 656 mg) was dissolved in 20 mL of methanol to obtain solution-B. Solution-A was added to solution-B and the mixed solution was stirred for 24 h. Subsequently, the white dispersion compound was centrifuged and washed with methanol thoroughly by centrifuging time and again. Then the solid was activated by heating at 100°C in an oven for 12 h, to obtain ZIF-8. ZIF-8 (12 mg) was dispersed in 20 mL of acetonitrile. Two drops of this dispersed solution were cast on a separator, and the amount of ZIF-8 loading was maintained at 0.015 mg. The separator was dried in a hot air oven at 70°C for 12 h, and the ensuing ZIF-8@separator was used in the ZIB. Scheme 1 illustrates the synthesis of various materials and the ZIB.

Fabrication of ZIBs and instrumental methods

ZnV_2O_4 , textured carbon, carbon black and PVDF were taken in the following weight ratios separately: 80:0:10:10, 70:10:10:10 and 60:20:10:10. All these mixed materials were ground well using a mortar-pestle assembly independently, and two different thick slurries were prepared by using a small amount of N-methyl pyrrolidone (NMP) in each and every case and coated immediately on circular shaped stainless steel (SS) electrodes (diameter: 1.5 cm) with the assistance of an OHP plastic sheet. The coated SS electrodes were vacuum dried for 12 h at 60°C. These electrodes were labelled as cathodes and the masses of the loaded materials were maintained in between $1.5\text{--}2 \text{ g cm}^{-2}$ in each and every case. Zn metal foil was cut by maintaining the same diameter of 1.5 cm and used as an anode. A few drops of an organic electrolyte solution of 0.5 M $\text{Zn}(\text{CF}_3\text{SO}_3)_2$ in acetonitrile were applied over GF/D borosilicate glass fiber separator, which was cut by an electrode cutter into circular disks of 1.5 cm diameter. For all cells, except the cell with ZIF-8 layer, this separator/electrolyte assembly was sandwiched between the pristine ZnV_2O_4 or $\text{ZnV}_2\text{O}_4@\text{TC}$ (3:1)



Scheme 1. Schematic showing the preparation of ZnV_2O_4 , TC and ZIF-8.

composite based cathodes and the Zn-anode. An additional ZIB wherein the electrolyte was applied over ZIF-8@separator, was also fabricated with the following configuration: SS/ZnV₂O₄/TC (3:1) composite-ZIF-8@separator/Zn. ZIBs were fabricated inside an argon filled MBraun Labstar glove box operating at O₂ and moisture levels of 0.5 and 0.5 ppm. Swagelok cells were employed for ZIB fabrication. Scheme 1 provides the synthetic methodology for the materials and the full cell. For capacity calculation of the ZIB with the ZIF-8 MOF, the weight of the coated MOF was also considered.

Instrumental techniques

Galvanostatic charge-discharge (GCD) measurements were performed on an Arbin instruments BT-2000 battery tester. Autolab PGSTAT 302 N potentiostat/galvanostat, furnished with a NOVA 1.9 software, and a frequency response analyzer (FRA) was used for cyclic voltammetry (CV), linear sweep voltammetry (*I*-*V*) and electrochemical impedance spectroscopy (EIS). For EIS, an ac perturbation potential of 20 mV was superimposed over the open-circuit dc potential of the cell, and measurements were done over a frequency range of 1 MHz to 0.01 Hz. Powder XRD data were recorded on a PANalytical, X'PertPRO instrument with a Cu-K α ($\lambda = 1.5406 \text{ \AA}$) radiation as the X-ray source. A Bruker Senterra dispersive micro Raman spectrometer with a 532 nm laser was used for recording the Raman spectra. Surface morphology analysis was carried out on a field emission-scanning electron microscope (FE-SEM: JEOL-JSM-7800). X-ray photoelectron spectra (XPS) were recorded on an Axis Supra K-ALPHA surface analysis spectrometer having a monochromatic, micro-focused Al-K α radiation (1486.6 eV). The instrument was run at a base pressure of $\sim 5 \times 10^{-11}$ Torr. Survey and core level spectra were collected at resolutions of 1 and 0.1 eV and with pass energies of 160 and 80 eV. All core-level spectra were deconvoluted by employing a non-linear iterative least-squares Gaussian-Lorentzian fitting procedure. Corrections due to charging effects were accounted for by using C(1 s) as an internal reference and the Fermi edge of a gold sample. A Jandel Peak FitTM (version 4.01) program was used for the analysis. Transmission electron microscopy (TEM) images were obtained on a JEOL 2100 microscope operating at an accelerating voltage of 200 kV using specimens coated over carbon-coated copper grids by employing the suspension and evaporation technique. Optical microscopy was done on a Carl Zeiss microscope with Imager.M2 m Axio Cam MRc5. Brunauer-Emmett-Teller (BET) surface area- and Barrett-Joyner-Halenda (BJH) pore size- analysis were performed for TC under a N2 environment at ~ 77 K, after degassing at 300 °C for 6 h.

Acknowledgements

Financial support for this work from Science & Engineering Research Board (SERB) of India (Grant no. CRG/2020/000482) is gratefully acknowledged by M.D. and S.N. S.N. is thankful to CSIR for the grant of junior research fellowship.

Conflict of Interest

The authors declare no conflict of interest.

Data Availability Statement

The data that support the findings of this study are available on request from the corresponding author. The data are not publicly available due to privacy or ethical restrictions.

Keywords: battery · capacity · metal-organic framework · zinc vanadate; zinc-ion

- [1] G. Fang, J. Zhou, A. Pan, S. Liang, *ACS Energy Lett.* **2018**, *3*, 2480–2501.
- [2] A. Konarov, N. Voronina, J. H. Jo, Z. Bakenov, Y. K. Sun, S. T. Myung, *ACS Energy Lett.* **2018**, *3*, 2620–2640.
- [3] X. Wang, Z. Zhang, B. Xi, W. Chen, Y. Jia, J. Feng, S. Xiong, *ACS Nano* **2021**, *15*, 9244–9272.
- [4] J. Wen, Y. Yu, C. Chen, *Mater. Express.* **2012**, *2*, 197–212.
- [5] Y. Sun, P. Shi, H. Xiang, X. Liang, Y. Yu, *Small.* **2019**, *15*, 1805479.
- [6] R. Guo, L. Ni, H. Zhang, X. Gao, R. Momen, A. Massoudi, G. Zou, H. Hou, X. Ji, *ACS Appl. Energ. Mater.* **2021**, *4*, 10940–10947.
- [7] S. Kumar, V. Verma, R. Chua, H. Ren, P. Kidkhunthod, C. Rojviriya, S. Sattayaporn, F. M. F. de Groot, W. Manalastas Jr., M. Srinivasan, *Batteries & Supercaps* **2020**, *3*, 619–630.
- [8] D. Zhang, J. Cao, X. Zhang, N. Insin, S. Wang, J. Han, Y. Zhao, J. Qin, Y. Huang, *Adv. Funct. Mater.* **2021**, *31*, 2009412.
- [9] X. Wang, B. Xi, X. Ma, Z. Feng, Y. Jia, J. Feng, Y. Qian, S. Xiong, *Nano Lett.* **2020**, *20*, 2899–2906.
- [10] Y. Tian, Y. An, H. Wei, C. Wei, Y. Tao, Y. Li, B. Xi, S. Xiong, J. Feng, Y. Qian, *Chem. Mater.* **2020**, *32*, 4054–4064.
- [11] Y. Zeng, X. F. Lu, S. L. Zhang, D. Luan, S. Li, X. W. Lou, (David) *Angew. Chem. Int. Ed.* **2021**, *60*, 22189–22194.
- [12] T. Cao, F. Zhang, M. Chen, T. Shao, Z. Li, Q. Xu, D. Cheng, H. Liu, Y. Xia, *ACS Appl. Mater. Interfaces* **2021**, *13*, 26924–26935.
- [13] W. Deng, Z. Li, Y. Ye, Z. Zhou, Y. Li, Zhang, M. Yuan, X. Hu, J. Zhao, W. Huang, Z. Li, C. Chen, H. Zheng, J. Li, *Adv. Energy Mater.* **2021**, *11*, 2003639.
- [14] Z. Li, T. Liu, R. Meng, L. Gao, Y. Zou, P. Peng, Y. Shao, X. Liang, *Energy Environ. Mater.* **2021**, *4*, 111–116.
- [15] L. Wang, K. W. Huang, J. Chen, J. Zheng, *Sci. Adv.* **2019**, *5*, eaax4279.
- [16] F. Ming, H. Liang, Y. Lei, S. Kandambeth, M. Eddaoudi, H. N. Alshareef, *ACS Energy Lett.* **2018**, *3*, 2602–2609.
- [17] V. Soundharajan, B. Sambandam, S. Kim, M. H. Alfaruqi, D. Y. Putro, J. Jo, S. Kim, V. Mathew, Y. K. Sun, J. Kim, *Nano Lett.* **2018**, *18*, 2402–2410.
- [18] N. Zhang, Y. Dong, M. Jia, X. Bian, Y. Wang, M. Qiu, J. Xu, Y. Liu, L. Jiao, F. Cheng, *ACS Energy Lett.* **2018**, *3*, 1366–1372.
- [19] Y. Tao, D. Huang, H. Chen, Y. Luo, *ACS Appl. Mater. Interfaces* **2021**, *13*, 16576–16584.
- [20] F. Wan, L. Zhang, X. Dai, X. Wang, Z. Niu, J. Chen, *Nat. Commun.* **2018**, *9*, 1656.
- [21] Z. Zhang, B. Xi, X. Wang, X. Ma, W. Chen, J. Feng, S. Xiong, *Adv. Funct. Mater.* **2021**, *31*, 2103070.
- [22] D. Kundu, S. H. Vajargah, L. Wan, B. Adams, D. Prendergast, L. F. Nazar, *Energy Environ. Sci.* **2018**, *11*, 881–892.
- [23] Y. Liu, C. Li, J. Xu, M. Ou, C. Fang, S. Sun, Y. Qiu, J. Peng, G. Lu, Q. Li, J. Han, Y. Huang, *Nano Energy* **2020**, *67*, 104211.
- [24] D. Zhang, J. Zhang, M. Pan, Y. Wang, T. Sun, J. Alloys Compd. **2021**, *853*, 157368.
- [25] M. Jiang, X. Cao, D. Zhu, Y. Duan, J. Zhang, *Electrochim. Acta* **2016**, *196*, 699–707.
- [26] Y. Gao, J. Wu, W. Zhang, Y. Tan, J. Zhao, B. Tang, *Mater. Lett.* **2014**, *128*, 208–211.
- [27] L. M. Z. De Juan-Corpuz, M. T. Nguyen, R. D. Corpuz, T. Yonezawa, N. C. Rosero-Navarro, K. Tadanaga, T. Tokunaga, S. Kheawhom, *ACS Appl. Nano Mater.* **2019**, *2*, 4247–4256.
- [28] F. K. Butt, M. Tahir, C. Cao, F. Idrees, R. Ahmed, W. S. Khan, Z. Ali, N. Mahmood, M. Tanveer, A. Mahmood, I. Aslam, *ACS Appl. Mater. Interfaces* **2014**, *6*, 13635–13641.
- [29] F. Duan, W. Dong, D. Shi, M. Chen, *Appl. Surf. Sci.* **2011**, *258*, 189–195.
- [30] M. Singha, R. Gupta, *Phys. B* **2019**, *563*, 101–106.
- [31] A. C. Ferrari, J. Robertson, *Phys. Rev. B* **2000**, *61*, 14095–14107.
- [32] H. Wang, T. Zhang, Z. Mao, X. Shi, J. Jin, B. He, R. Wang, Y. Gong, *Energy Environ. Sci.* **2022**, Advance article.

- [33] R. Fei, H. Wang, Q. Wang, R. Qiu, S. Tang, R. Wang, B. He, Y. Gong, H. J. Fan, *Adv. Energy Mater.* **2020**, *10*, 2002741.
- [34] H. Geng, M. Cheng, B. Wang, Y. Yang, Y. Zhang, C. C. Li, *Adv. Funct. Mater.* **2020**, *30*, 1907684.
- [35] Y. R. Lee, M. S. Jang, H. Y. Cho, H. J. Kwon, S. Kim, W. S. Ahn, *Chem. Eng. J.* **2015**, *271*, 276–280.
- [36] A. Samadi-Maybodi, S. Ghasemi, H. Ghaffari-Rad, *J. Power Sources* **2016**, *303*, 379–387.
- [37] H. Alamgholiloo, S. Rostamnia, A. Hassankhani, R. Banaei, *Synlett* **2018**, *29*, 1593–1596.
- [38] H. Wang, Y. Wang, A. Jia, C. Wang, L. Wu, Y. Yang, Y. Wang, *Catal. Sci. Technol.* **2017**, *7*, 5572–5584.
- [39] Q. Li, K. Ma, G. Yang, C. Wang, *Energy Storage Mater.* **2020**, *29*, 246–253.
- [40] Q. Li, K. Ma, C. Hong, G. Yang, C. Wang, *Sci. China Mater.* **2021**, *64*, 1386–1395.
- [41] G. Wang, B. Kohn, U. Scheler, F. Wang, S. Oswald, M. Löfller, D. Tan, P. Zhang, J. Zhang, X. Feng, *Adv. Mater.* **2020**, *32*, 1905681.
- [42] S. D. Han, S. Kim, D. Li, V. Petkov, H. D. Yoo, P. J. Phillips, H. Wang, J. J. Kim, K. L. More, B. Key, R. F. Klie, J. Cabana, V. R. Stamenkovic, T. T. Fister, N. M. Markovic, A. K. Burrell, S. Tepavcevic, J. T. Vaughey, *Chem. Mater.* **2017**, *29*, 4874–4884.
- [43] M. Wang, A. Emre, S. Tung, A. Gerber, D. Wang, Y. Huang, V. Cecen, N. A. Kotov, *ACS Nano* **2019**, *13*, 1107–1115.
- [44] L. Ma, S. Chen, H. Li, Z. Ruan, Z. Tang, Z. Liu, Z. Wang, Y. Huang, Z. Pei, J. A. Zapien, C. Zhi, *Energy Environ. Sci.* **2018**, *11*, 2521–2530.
- [45] C. Pan, R. Zhang, R. G. Nuzzo, A. A. Gewirth, *Adv. Energy Mater.* **2018**, *8*, 1800589.
- [46] Y. Lu, T. Zhu, N. Xu, K. Huang, *ACS Appl. Energ. Mater.* **2019**, *2*, 6904–6910.

Manuscript received: November 25, 2021

Revised manuscript received: December 13, 2021

Accepted manuscript online: December 16, 2021

Version of record online: December 30, 2021